The International Journal of Advanced Manufacturing Technology (2018) 95:2421–2428
https://doi.org/10.1007/s00170-017-1387-6

ORIGINAL ARTICLE

# Numerical and experimental investigations of variable polarity gas tungsten arc welding

L. L. Wang[1] · J. H. Wei[1] · Z. M. Wang[1]

Received: 27 July 2017 / Accepted: 13 November 2017 / Published online: 23 November 2017


**Abstract**
Variable polarity gas tungsten arc welding (VP-GTAW) has been suggested as a feasible method for welding aluminum alloys due to the enhanced surface cleaning of the oxide film. However, the principles governing the correlations between the electrode positive (EP) ratio, weld geometry, and weld microstructure are not well understood. Therefore, experiments with different EP ratios but same welding current were conducted. A three-dimensional heat transfer and fluid flow model of VP-GTAW was developed with validation against experimental results. Solidification parameters such as the temperature gradient, solidification growth rate, and cooling rate were computed from the model. The results indicate that VP-GTAW produces nearly defect-free joints. Both the top weld width and bottom weld width decrease with increasing EP ratio due to the decreased heat input. The bottom weld width is greater than the minimum weld profile width in the middle of the plate, which indicates that the Marangoni stress has a significant effect on the convective heat transfer and weld geometry. Variable grain dimensions are produced by different EP ratios at the same welding current. Weld pool oscillation originated from the alternating arc force plays a dominant role in the grain dimension.

**Keywords** Variable polarity welding · Numerical simulation · Weld geometry · Cooling rate · Grain dimension

## 1 Introduction

Lightweight engineering alloys have been widely used in the automotive and aerospace sectors to conserve energy and promote maneuverability, and welding is an essential procedure in the fabrication of automotive and aerospace structures [1, 2]. Lightweight aluminum alloys are widely adopted due to their ultra-low density, corrosion resistance properties, and acceptable mechanical properties [3, 4]. However, due to the existence of a heat-resistant oxide film on the surface of aluminum alloys, defects such as lack of fusion, bead irregularity, and oxide inclusions commonly form during the conventional welding process. Variable polarity gas tungsten arc welding (VP-GTAW) has recently been suggested as a feasible method for the welding of aluminum alloys. VP-GTAW features low heat input characteristics and enhanced surface cleaning of the oxide film during welding of aluminum alloys [5]. A schematic diagram of the current waveform of VP-GTAW is shown in Fig. 1. The welding current consists of a negative current during the electrode negative (EN) phase and a positive current during the electrode positive (EP) phase [6]. The aluminum oxide film is eliminated during the EP phase, and the EP ratio is generally less than 50% [7].

VP-GTAW has been the subject of numerous studies. Yarmuch and Patchett [8] studied the effect of the EP ratio on the weld penetration and bead width. Dutra et al. [9] conducted experiments to determine the effect of the EP time on cathodic cleaning, arc voltage, arc power, and weld bead geometry during VP-GTAW of an aluminum alloy. Pan et al. [10] numerically investigated the weld pool behavior and weld bead formation during VP-GTAW. Babu and Cross [11] investigated the effect of regular and modified VP-GTAW on grain refinement during the welding of magnesium alloys. Wang et al. [12] observed that double pulsed gas tungsten arc welding (GTAW) produced finer dendrites than those produced by conventional pulsed GTAW. The literature reveals that the previous work can be divided into two categories: (1) studies of the effect of the EP time or ratio on the weld pool behavior and weld bead dimensions and (2) comparisons of the microstructure or macrostructure in the fusion zone produced by VP-GTAW and modified VP-GTAW. However, the principles governing the correlations between the EP ratio, weld geometry, and weld microstructure are not well understood.

✉ Z. M. Wang
wangzhm@scut.edu.cn
[1] School of Mechanical and Automotive Engineering, South China University of Technology, Guangzhou 510641, China

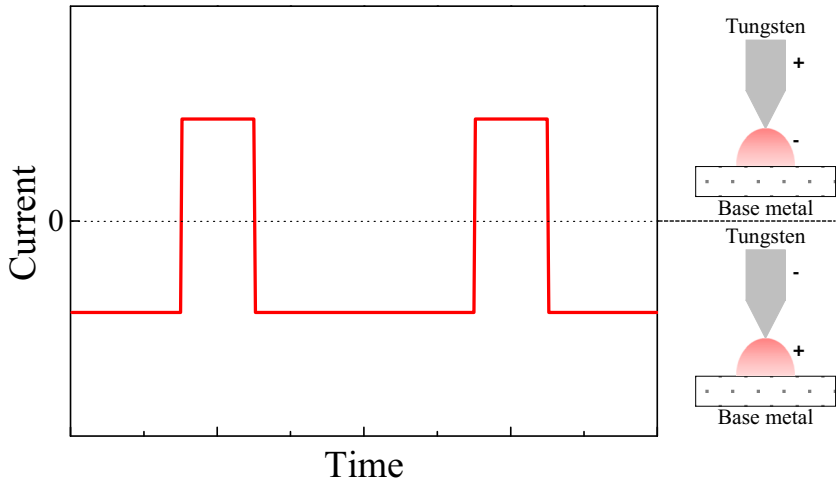


**Fig. 1** Schematic diagram of the current waveform of variable polarity GTAW

The welding current is known to be an important variable in GTAW. A reduction of the welding current results in a smaller weld pool, a narrower heat-affected zone, and improved weld quality. The results of VP-GTAW with different EP ratios but the same welding current remain unknown and were investigated in this research. First, three experiments with different EP ratios but the same welding current were conducted. Then, a three-dimensional heat transfer and fluid flow model of VP-GMAW was developed and validated against the experimental data. The grain morphology and dimensions were controlled by the solidification parameters (i.e., the temperature gradient ($G$), solidification growth rate ($R$), $G/R$, and $GR$ [13, 14]), which were computed from the model. Variable grain dimensions are generated by different EP ratios at the same welding current, and the mechanism of this phenomenon is revealed.

## 2 Materials and methods

### 2.1 Experimental procedure

A sample of 1060 aluminum alloy with dimensions of 250 × 100 × 4 $mm^3$ was used as the base metal. Table 1 shows the chemical compositions of AA1060 aluminum. Argon was used as the shielding gas, and the joint type was bead-on-plate welding.

A self-developed welding power supply with a variable polarity current was used in this study. The welding parameters are presented in Table 2. All of the experiments were conducted with the same welding current (170 A), whereas the EP ratio increased from 20 to 25 and 30%.

After welding, the welds were cut along a transverse-section to obtain the weld geometry. The specimens were then ground and polished to 0.06 μm using colloidal silica. Metallographic images were taken using a polarized microscope after electrolytic etching by standard Barker's reagent.

**Table 1** Chemical compositions of AA1060 (base metal) (wt%)

| Material | Fe | Si | Cu | V | Zn | Mg | Mn | Ti | Al |
|---|---|---|---|---|---|---|---|---|---|
| AA1060 | 0.35 | 0.25 | 0.05 | 0.05 | 0.05 | 0.03 | 0.03 | 0.03 | Bal. |

### 2.2 Numerical methods

#### 2.2.1 Heat transfer and fluid flow in the weld pool

The heat transfer and fluid flow in the weld pool were calculated by solving the equations for the conservation of mass, momentum, and energy in three dimensions [15]. The model considers the effect of the Marangoni stress, electromagnetic force, and buoyancy on liquid metal convection within the weld pool [16]. The molten metal is assumed to be an incompressible, laminar, and Newtonian fluid. The molten metal flow in the weld pool can be expressed by the following momentum conservation eq. [17]:

**Table 2** Parameters of the welding process

| Process parameters | No. 1 | No. 2 | No. 3 |
|---|---|---|---|
| EP ratio (%) | 20 | 25 | 30 |
| Mean current (A) | 170 | 170 | 170 |
| Welding speed (mm $s^{-1}$) | 2.5 | 2.5 | 2.5 |
| Current period (ms) | 20 | 20 | 20 |
| Current during EN (A) | 150 | 175 | 200 |
| Voltage during EN (V) | 13 | 13.5 | 14 |
| EN duration (ms) | 16 | 15 | 14 |
| Current during EP (A) | 250 | 155 | 100 |
| Voltage during EN (V) | 26.6 | 22.4 | 20 |
| EP duration (ms) | 4 | 5 | 6 |

$$\rho\frac{\partial u_j}{\partial t}+\rho\frac{\partial\left(u_i u_j\right)}{\partial x_i}=\frac{\partial}{\partial x_i}\left(\mu\frac{\partial u_j}{\partial x_i}\right)+S_j \tag{1}$$

where $\rho$ is the density, $t$ is the time, $x_i$ is the distance in the $i$th ($i = 1$, 2, and 3) orthogonal direction, $u_j$ is the velocity component in the $j$ direction, $\mu$ is the effective viscosity, and $S_j$ is the source terms for the $j$th momentum equation and is given as [18]:

$$S_j=-\frac{\partial p}{\partial x_j}+\frac{\partial}{\partial x_j}\left(\mu\frac{\partial u_j}{\partial x_j}\right)-C\left(\frac{(1-f_{\mathrm{L}})^2}{f_{\mathrm{L}}{}^3+B}\right)u_j-\rho U\frac{\partial u_j}{\partial x_j}+\rho g\beta(T-T_{\mathrm{r}}) \tag{2}$$

where $p$ represents the pressure, $U$ is the welding speed, $T_{\mathrm{r}}$ is a reference temperature, $\beta$ is the coefficient of volume expansion, the third term represents the frictional dissipation in the mushy zone according to the Carman–Kozeny equation for flow through porous media [19], $f_{\mathrm{L}}$ is the liquid fraction, $B$ is a very small computational constant to avoid division by zero, and $C$ is a constant that accounts for the morphology of the mushy zone ($1.6\times10^4$). The fourth term accounts for the relative motion between the heat source and the workpiece, and the last term is the buoyancy source term.The following continuity equations are solved in conjunction with the momentum equation to obtain the pressure field.

$$\frac{\partial(\rho u_i)}{\partial x_i}=0 \tag{3}$$

To trace the weld pool's liquid/solid interface, the total enthalpy $H$ is represented by the sum of the sensible heat $h$ and the latent heat content $\Delta H$ (i.e., $H = h + \Delta H$) [20]. The sensible heat $h$ is expressed as $h=\int C_p dT$, where $C_p$ is the specific heat and $T$ is the temperature. The latent heat content $\Delta H$ is given as $\Delta H = f_{\mathrm{L}}L$, where $L$ is the latent heat of fusion. For simplicity, the liquid fraction $f_{\mathrm{L}}$ is assumed to vary linearly with temperature and is given as [21]:

$$f_{\mathrm{L}}=\begin{cases}1 & T>T_{\mathrm{L}}\\ \dfrac{T-T_{\mathrm{S}}}{T_{\mathrm{L}}-T_{\mathrm{S}}} & T_{\mathrm{S}}\le T<T_{\mathrm{L}}\\ 0 & T<T_{\mathrm{S}}\end{cases} \tag{4}$$

where $T_{\mathrm{L}}$ and $T_{\mathrm{S}}$ are the liquidus and solidus temperatures, respectively. Thus, the transportation of thermal energy in the weld workpiece can be expressed by the following modified energy equation: [21]

$$\rho\frac{\partial h}{\partial t}+\rho\frac{\partial(u_i h)}{\partial x_i}=\frac{\partial}{\partial x_i}\left(\frac{k}{C_p}\frac{\partial h}{\partial x_i}\right)+S_h \tag{5}$$

where $k$ is the thermal conductivity, and the source term $S_h$ is due to the latent heat content and is expressed as [22]:

$$S_h=-\rho\frac{\partial(\Delta H)}{\partial t}-\rho\frac{\partial(u_i\Delta H)}{\partial x_i}-\rho U\frac{\partial h}{\partial x_i}-\rho U\frac{\partial\Delta H}{\partial x_i} \tag{6}$$

The heat transfer and fluid flow equations are solved for the complete workpiece. The boundary conditions and corresponding equations can be found in the literature and are not shown here [17, 18]. During VP-GTAW, the arc efficiency of the EN phase is different from that of the EP phase. Cantin and Francis [23] determined that the arc efficiency ranged from 0.76 to 0.89 for the EN polarity and 0.52 to 0.63 for the EP polarity. Furthermore, the suggested arc efficiency of VP-GTAW with an EP ratio of 25% is 0.72. Therefore, the arc efficiency is set to 0.72 in this study. The data used for the calculations of the weld pool temperature and velocity fields are shown in Table 3 [24].

### 2.2.2 Calculation of the solidification parameters

The temperature gradient ($G$) and solidification growth rate ($R$) are calculated at the top of the weld pool for the microstructural evaluation. The solidification direction is assumed to be parallel to the local maximum heat flow direction on the trailing side of the weld pool. The heat flow direction at any location on the S/L interface of the molten pool is normal to the interface and can be calculated by [25, 26]:

$$\nabla T=\frac{\partial T}{\partial x}i+\frac{\partial T}{\partial y}j+\frac{\partial T}{\partial z}k \tag{7}$$

where $T$ is the temperature, and $i$, $j$, and $k$ are the unit vectors in the welding direction, $x$, the width direction, $y$, and the vertical depth direction, $z$, respectively. The temperature gradient G is calculated by:

$$G=\|\nabla T\| \tag{8}$$

**Table 3** Data used for the calculations of the weld pool temperature and velocity fields

| Variables and units | AA1060 |
|---|---|
| Density of the liquid metal (kg $m^{-3}$) | 2400 |
| Viscosity of the liquid (kg $m^{-1}$ $s^{-1}$) | 0.001 |
| Solidus temperature (K) | 919 |
| Liquidus temperature (K) | 930 |
| Enthalpy of the solid at the melting point (J $kg^{-1}$) | $6.25\times10^5$ |
| Enthalpy of the liquid at the melting point (J $kg^{-1}$) | $9.98\times10^5$ |
| Specific heat of the solid (J $kg^{-1}$ $K^{-1}$) | 900 |
| Specific heat of the liquid (J $kg^{-1}$ $K^{-1}$) | 1170 |
| Thermal conductivity of the solid (W $m^{-1}$ $K^{-1}$) | 168 |
| Thermal conductivity of the liquid (W $m^{-1}$ $K^{-1}$) | 108 |
| Coefficient of thermal expansion ($K^{-1}$) | $2.375\times10^{-5}$ |
| Temperature coefficient of surface tension (N $m^{-1}$ $K^{-1}$) | $-3.5\times10^{-4}$ |

The solidification growth rate is given as:

$$R = v\frac{\partial T/\partial x}{G} \tag{9}$$

where $v$ is the welding speed. The grain morphology and dimensions were dominated by G/R and GR, which were computed from the model.

## 3 Results and discussion

Figure 2 shows the weld beads produced by VP-GTAW with different EP ratios, and the corresponding process parameters are shown in Table 2. Defects such as bead irregularity and oxide inclusions are significantly mitigated. Nearly defect-free joints are produced, which provides additional evidence that VP-GTAW is a feasible method for welding aluminum alloys. With an increase of the EP ratio from 20 to 25 and 30%, the sufficient arc power decreases from 2080 to 1901 and 1843 W, respectively. As a result, the weld width decreases gradually from 10.1 to 9.3 and 8.2 mm.

Figure 3 shows the computed three-dimensional temperature and velocity fields in the weld pool. Each color in the weld pool represents a temperature range that can be determined from the legend. At the top surface of the weld pool, the liquid metal flows from the center to the edge and is mainly driven by the Marangoni stress, which results from the spatial gradient of the surface tension [27]. The liquid metal circulates in the weld pool with a maximum velocity of approximately 1 m $s^{-1}$. At this velocity, heat is transported within the weld pool mainly by convection rather than conduction.

The heat transfer and fluid flow model is validated by comparing the calculated and experimentally observed transverse sections of the weld, as shown in Fig. 4. Complete joint penetration welds are produced in all cases. The calculated weld width, root width, and weld geometry are reasonably consistent with the experimentally observed results. This agreement

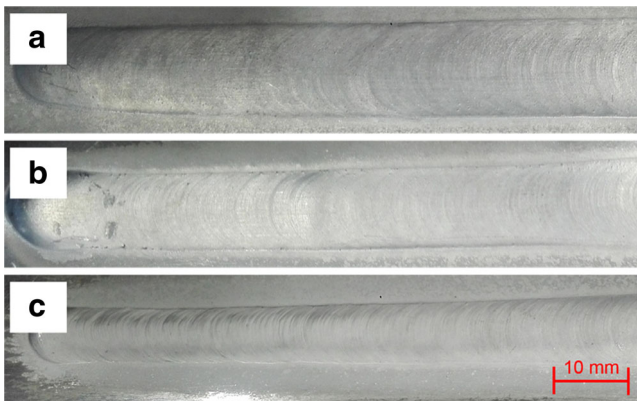


**Fig. 2** Weld beads produced by VP-GTAW with different EP ratios: **a** 20%, **b** 25%, and **c** 30%

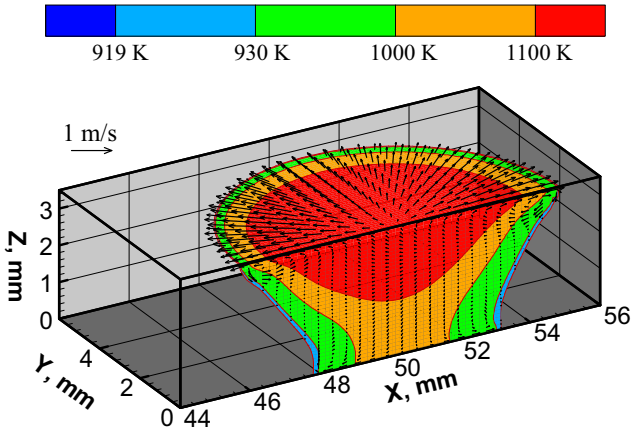


**Fig. 3** Computed three-dimensional temperature and velocity fields in the weld pool. The process parameters correspond to no. 2 in Table 2

indicates the validity of the modeling results, which are further used to compute the solidification parameters. At the top and bottom surfaces of the weld pool, liquid metal flows from the center to the edge of weld pool due to the Marangoni stress. As a result, the velocities of the liquid metal at the top and bottom surfaces are far higher than that in the middle of the plate, as shown in Fig. 4a. Furthermore, both the numerical and experimental results indicate that the bottom weld width is greater than the minimum weld width, which is located in the middle of the plate. Therefore, the reliability of the model is

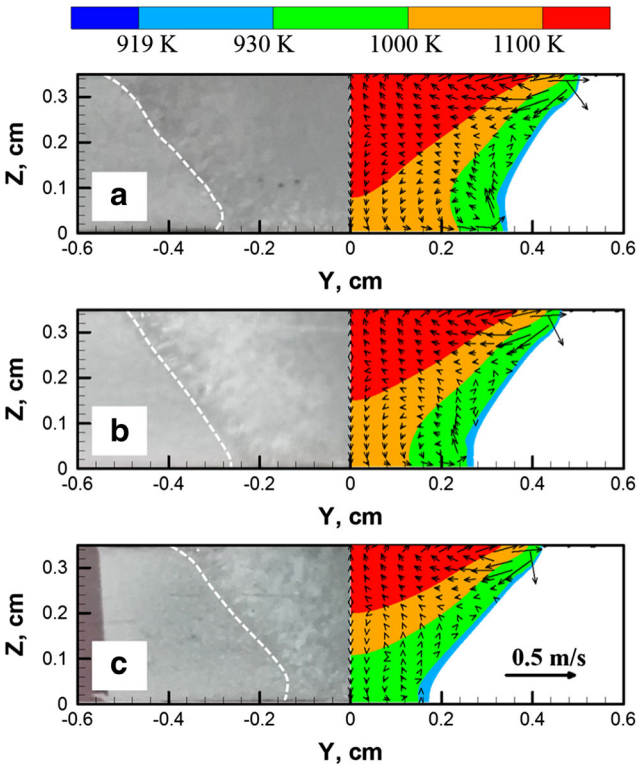


**Fig. 4** Validation of the model by comparing the calculated and experimentally observed transverse sections of the weld. **a** 20%, **b** 25%, **c** 30%

confirmed. If only a conduction heat transfer model is considered, the width of the weld profile decreases with increasing weld penetration. However, the width of the weld profile decreases and then increases with increasing weld penetration. The shape of the weld profile width is similar to that of the velocity, which reveals that the Marangoni stress has a significant effect on the heat distribution and weld geometry.

Figure 5 shows the weld dimensions produced by VP-GTAW with different EP ratios. Complete joint penetration welds are produced in all cases, so the weld penetrates the thickness of the base metal (3.5 mm). With an increase of the EP ratio from 20 to 25 and 30%, the sufficient arc power decreases from 2080 to 1901 and 1843 W, respectively. As a result, both the top weld width and bottom weld width decrease with increasing EP ratio. The half width of the bottom weld decreases significantly from 3.2 to 2.6 and 1.8 mm.

Figure 6 shows the spatial distribution of the *G*/*R* on the top surface of the welds. With increasing EP ratio from 20 to 25 and 30%, the sufficient arc power decreases from 2080 to 1901 and 1843 W, respectively; the heat input decreases with increasing EP ratio. The *G*/*R* increases gradually from the center of the weld to the edge in all cases. Smaller G/R have a higher tendency to produce equiaxed grains in the fusion zone. For 1060 aluminum with a welding speed of 2.5 mm $s^{-1}$, the columnar to equiaxed transformation (CET) occurs when the value of *G* is less than 30 K $mm^{-1}$ [28]; CET occurs only when the *G*/*R* is less than 12 K s $mm^{-2}$. The *G*/*R* value is greater than 12 K s $mm^{-2}$ in all of the cases. Therefore, equiaxed grains are not predicted to form in the fusion zone in any of the cases.

Figure 7 shows the macrostructures of the welds on the top surface. Different grains can be distinguished by the contrast in color. No porosity or solidification cracking is observed in the metallographic diagrams, which provide additional evidence that VP-GTAW is a feasible process for welding of aluminum. Columnar grains grow from the edge to the center, and no equiaxed grains are observed in the fusion zone. The

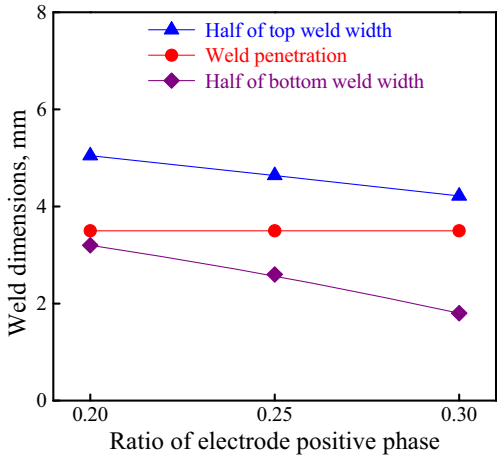


**Fig. 5** Weld dimensions of VP-GTAW

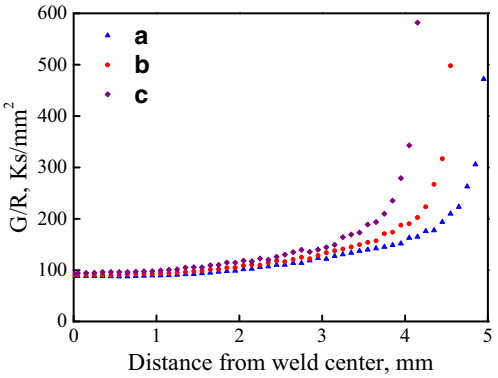


**Fig. 6** Spatial distribution of the *G*/*R* of VP-GTAW with different EP ratios: **a** 20%, **b** 25%, and **c** 30%

experimental results agree well with the predictions based on the computed data.

In addition, variable grain dimensions are produced by different EP ratios at the same welding current. Table 4 shows the grain dimensions produced by VP-GTAW with different EP ratios. The grain dimensions are measured at the top center surface of the welds. With increasing EP ratio from 20 to 25 and 30%, the grain size at the center of the VP-GTA welds increases from 276 ± 47 μm to 445 ± 33 μm and 379 ± 47 μm, respectively.

The grain dimensions are important for controlling the welding quality, and finer grains indicate better mechanical properties [29]. Therefore, the mechanism of this phenomenon is investigated in the following paragraphs to achieve grain refinement. Figure 8 shows spatial distribution of Vickers hardness along transverse section of the fusion zone. Vickers hardness of the fusion zone decreases when EP ratio increases from 20 to 25%; Vickers hardness of the fusion zone increases when EP ratio increases from 25 to 30%. The variation of Vickers hardness shows good agreement with variation of grain dimension in the fusion zone.

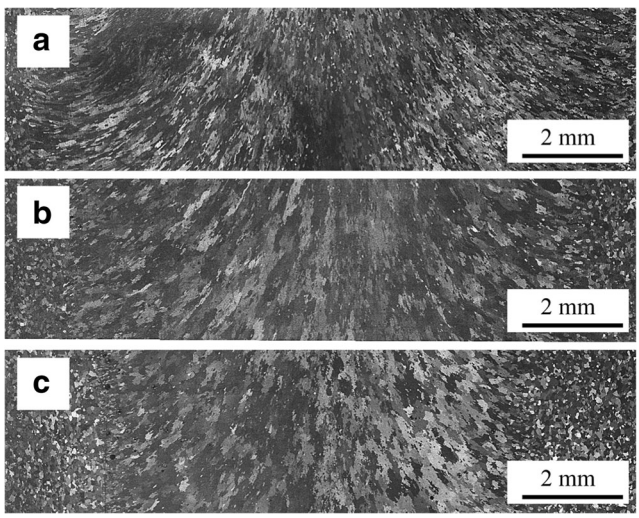


**Fig. 7** Macrostructures of the top surfaces of the welds. **a** 20%, **b** 25%, **c** 30%

**Table 4** Mean grain dimensions produced by VP-GTAW with different EP ratios

| EP ratio (%) | Welding current (A) | Grain dimension (μm) |
|---|---|---|
| 20 | 170 | 276 ± 47 |
| 25 | 170 | 445 ± 33 |
| 30 | 170 | 379 ± 47 |

Figure 9 shows the spatial distribution of the cooling rate (*GR*) on the top surface of the welds with different EP ratios. GR decreases gradually from the weld center to the edge in all cases, which indicates that smaller grains are produced in the center of the fusion zone. This result is consistent with the experimental results. With increasing EP ratio from 20 to 25 and 30%, *GR* at the center of the top surface increases slightly from 553 to 569 and 588 K $s^{-1}$, respectively. This change in the cooling rate is so insignificant that its effect on the grain dimensions is negligible.Another factor that can change the grain dimensions is the weld pool oscillation, which occurs due to the alternating arc force [30]. The relation between the arc force ($F_A$) and welding current ($I$) is given as [31]:

$$F_A = \frac{\mu_0 I^2}{8\pi}\left(1 + 2ln\left(\frac{R_2}{R_1}\right)\right) \quad (10)$$

where $\mu_0$ is the magnetic permeability, $R_1$ is the radius of the arc at the welding electrode, and $R_2$ is the radius of the arc at the base plate. The negative current during the EN phase and the positive current during the EP phase are not the same. However, the orientations of the arc forces generated during the EP and EN phases are the same. Figure 10 shows a schematic diagram of the arc force on the weld pool. The orientation of the arc force is from the electrode to the base plate [32].The arc force can be approximated as being linearly related to the square of the arc current [33]:

$$F_A = C_f I^2 \quad (11)$$

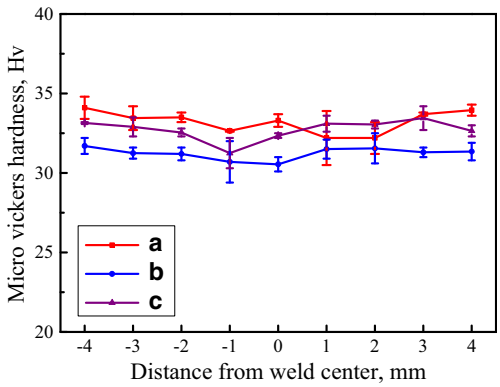


**Fig. 8** Spatial distribution of Vickers hardness along transverse section of the fusion zone. **a** 20%. **b** 25%. **c** 30%

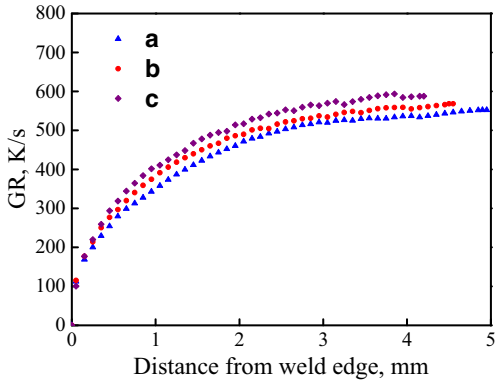


**Fig. 9** Spatial distribution of the cooling rate (*GR*) of VP-GTAW with different EP ratios: **a** 20%, **b** 25%, and **c** 30%

where the proportionality factor $C_f$ between the arc force and the square of the current is $7.25 \times 10^{-8}$ N $A^{-2}$. A puddle surface is produced by this arc force. The shape of the puddle surface remains constant when the value of the arc force is static. Once the arc force begins alternating, the shape of the puddle surface oscillates, which is called weld pool oscillation. The weld pool oscillation increases with increasing amplitude of the arc force. When the EP ratio increases from 20 to 25 and 30%, the amplitude of arc force is 2.9, 0.5, and 2.2 mN, respectively. Therefore, the maximum weld pool oscillation occurs with an EP ratio of 20%, and the minimum weld pool oscillation occurs with an EP ratio of 25%.

More dendrite fragmentations are produced in the mushy zone due to enhanced weld pool oscillation during VP-GTAW with an EP ratio of 20%. If the dendrite fragments can survive the high temperature of the weld pool, they act as nucleation sites for new grains. Grain refinement is achieved due to the increased number of nucleation sites. In this manner, the smallest grains are produced with an EP ratio of 20%, and the largest grains are produced with an EP ratio of 25%. This quantitative analysis is consistent with the experimental results shown in Table 4. In summary, during VP-GTAW with different EP ratios and the same welding current, weld pool

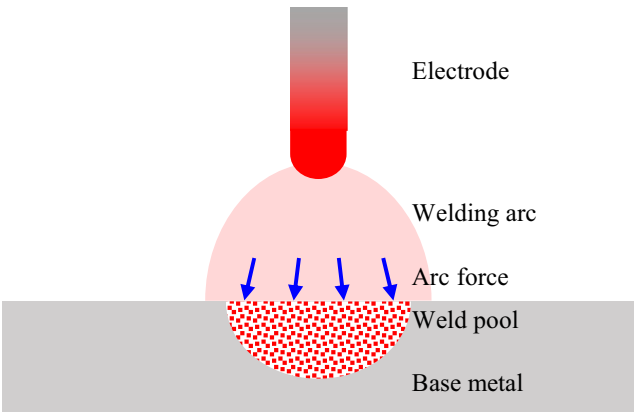


**Fig. 10** Schematic diagram of the arc force on the weld pool

oscillation due to the alternating arc force plays a dominant role in the grain dimensions.

## 4 Conclusions

This study develops a three-dimensional heat transfer and fluid flow model for VP-GTAW with complete joint penetration. The process and solidification structure of VP-GTAW with different EP ratios and the same welding current are studied numerically and experimentally. The specific findings are as follows.

(1) VP-GTAW produces nearly defect-free joints, which provides additional evidence that VP-GTAW is a feasible method for welding aluminum alloys.
(2) The numerical and experimental results both indicate that the bottom weld width is greater than the minimum weld width at the middle of the plate due to the Marangoni stress.
(3) The heat input decreases with increasing EP ratio at the same welding current. As a result, the top weld width and bottom weld width both decrease with increasing EP ratio.
(4) Variable grain dimensions and Vickers hardness in the fusion zone are produced by different EP ratios at the same welding current. Weld pool oscillation originated from alternating arc force plays a dominant role in the grain dimensions.

**Acknowledgements** The authors are grateful for the financial support for this research from the National Natural Science Foundation of China (No. 51375173) and the Science and Technology Programs of Guangdong Province (Nos. 2014B010104002 and 2016B090927008).

**Compliance with ethical standards**

**Conflict of interest** The authors declare that they have no conflict of interest.

## References

1. Li J, Li H, Wei H, Ni Y (2016) Effect of pulse on pulse frequency on welding process and welding quality of pulse on pulse MIG welding-brazing of aluminum alloys to stainless steel. Int J Adv Manuf Technol 87(1):51–63. https://doi.org/10.1007/s00170-016-8369-y
2. Wang LL, Heng GC, Chen H, Xue JX, Lin FL, Huang WJ (2016) Methods and results regarding sinusoid modulated pulse gas metal arc welding. Int J Adv Manuf Technol 86(5):1841–1851. https://doi.org/10.1007/s00170-015-8267-8
3. Dragatogiannis DA, Koumoulos EP, Kartsonakis IA, Pantelis DI, Karakizis PN, Charitidis CA (2016) Dissimilar friction stir welding between 5083 and 6082 Al alloys reinforced with TiC nanoparticles. Mater Manuf Process 31(16):2101–2114. https://doi.org/10.1080/10426914.2015.1103856
4. Li J, Li H, Huang C, Xiang T, Ni Y, Wei H (2017) Welding process characteristics of pulse on pulse MIG arc brazing of aluminum alloy to stainless steel. Int J Adv Manuf Technol 91(1):1057–1067. https://doi.org/10.1007/s00170-016-9820-9
5. Pan J, Hu S, Yang L, Li H (2016) Simulation and analysis of heat transfer and fluid flow characteristics of variable polarity GTAW process based on a tungsten–arc-specimen coupled model. Int J Heat Mass Transf 96:346–352. https://doi.org/10.1016/j.ijheatmasstransfer.2016.01.014
6. Song G, Wang P, Liu LM (2010) Study on ac-PMIG welding of AZ31B magnesium alloy. Sci Technol Weld Join 15(3):219–225. https://doi.org/10.1179/136217110x12665048207656
7. Cho J, Lee J-J, Bae S-H (2015) Heat input analysis of variable polarity arc welding of aluminum. Int J Adv Manuf Technol 81(5):1273–1280. https://doi.org/10.1007/s00170-015-7292-y
8. Yarmuch MAR, Patchett BM (2007) Variable AC polarity GTAW fusion behavior in 5083 aluminum. Weld J 86(7):196S–200S
9. Dutra JC, Cirino LM, Gonçalves e Silva RH (2010) AC–GTAW of aluminium—new perspective for evaluation of role of positive polarity time. Sci Technol Weld Join 15(7):632–637. https://doi.org/10.1179/136217110X12813393169570
10. Pan J, Hu S, Yang L, Wang D (2016) Investigation of molten pool behavior and weld bead formation in VP-GTAW by numerical modelling. Mater Des 111:600–607. https://doi.org/10.1016/j.matdes.2016.09.022
11. Babu NK, Cross CE (2012) Grain refinement of AZ31 magnesium alloy weldments by AC pulsing technique. Metall Mater Trans A 43A(11):4145–4154. https://doi.org/10.1007/s11661-012-1241-2
12. Wang Y, Qi B, Cong B, Yang M, Liu F (2017) Arc characteristics in double-pulsed VP-GTAW for aluminum alloy. J Mater Process Technol 249:89–95. https://doi.org/10.1016/j.jmatprotec.2017.05.027
13. DebRoy T, David SA (1995) Physical processes in fusion welding. Rev Mod Phys 67(1):85–112. https://doi.org/10.1103/RevModPhys.67.85
14. Wu C, Li S, Zhang C, Wang X (2016) Microstructural evolution in 316LN austenitic stainless steel during solidification process under different cooling rates. J Mater Sci 51(5):2529–2539. https://doi.org/10.1007/s10853-015-9565-0
15. Wang LL, Wei HL, Xue JX, DebRoy T (2017) A pathway to microstructural refinement through double pulsed gas metal arc welding. Scr Mater 134:61–65. https://doi.org/10.1016/j.scriptamat.2017.02.034
16. David SA, Debroy T (1992) Current issues and problems in welding science. Science 257(5069):497–502. https://doi.org/10.1126/science.257.5069.497
17. Mishra S, DebRoy T (2005) A heat-transfer and fluid-flow-based model to obtain a specific weld geometry using various combinations of welding variables. J Appl Phys 98(4):article number 044902. https://doi.org/10.1063/1.2001153
18. Roy GG, Elmer JW, DebRoy T (2006) Mathematical modeling of heat transfer, fluid flow, and solidification during linear welding with a pulsed laser beam. J Appl Phys 100(3):article number 034903. https://doi.org/10.1063/1.2214392
19. Voller VR, Prakash C (1987) A fixed grid numerical modelling methodology for convection-diffusion mushy region phase-change problems. Int J Heat Mass Transf 30(8):1709–1719. https://doi.org/10.1016/0017-9310(87)90317-6
20. Zhang W, Kim C-H, DebRoy T (2004) Heat and fluid flow in complex joints during gas metal arc welding—part I: numerical model of fillet welding. J Appl Phys 95(9):5210–5219. https://doi.org/10.1063/1.1699485

21. Wei HL, Blecher JJ, Palmer TA, Debroy T (2015) Fusion zone microstructure and geometry in complete-joint-penetration laser-arc hybrid welding of low-alloy steel. Weld J 94(4):135S–144S
22. Ribic B, Rai R, DebRoy T (2008) Numerical simulation of heat transfer and fluid flow in GTA/laser hybrid welding. Sci Technol Weld Join 13(8):683–693. https://doi.org/10.1179/136217108X356782
23. Cantin GMD, Francis JA (2005) Arc power and efficiency in gas tungsten arc welding of aluminium. Sci Technol Weld Join 10(2):200–210. https://doi.org/10.1179/174329305X37033
24. Wang LL, Wei HL, Xue JX, DebRoy T (2017) Special features of double pulsed gas metal arc welding. J Mater Process Technol 251:369–375. https://doi.org/10.1016/j.jmatprotec.2017.08.039
25. Wei HL, Elmer JW, DebRoy T (2016) Origin of grain orientation during solidification of an aluminum alloy. Acta Mater 115:123–131. https://doi.org/10.1016/j.actamat.2016.05.057
26. Wei HL, Mazumder J, DebRoy T (2015) Evolution of solidification texture during additive manufacturing. Sci Rep 5(1):16446. https://doi.org/10.1038/srep16446
27. Wei HL, Elmer JW, DebRoy T (2017) Crystal growth during keyhole mode laser welding. Acta Mater 133:10–20. https://doi.org/10.1016/j.actamat.2017.04.074
28. Schempp P, Rethmeier M (2015) Understanding grain refinement in aluminium welding. Weld World 59(6):767–784. https://doi.org/10.1007/s40194-015-0251-2
29. Zhang Z, Wu Q, Grujicic M, Wan ZY (2016) Monte Carlo simulation of grain growth and welding zones in friction stir welding of AA6082-T6. J Mater Sci 51(4):1882–1895. https://doi.org/10.1007/s10853-015-9495-x
30. Kumar R, Dilthey U, Dwivedi DK, Ghosh PK (2009) Thin sheet welding of Al 6082 alloy by AC pulse-GMA and AC wave pulse-GMA welding. Mater Des 30(2):306–313. https://doi.org/10.1016/j.matdes.2008.04.073
31. Lin ML, Eagar TW (1986) Pressures produced by gas tungsten arcs. Metall Trans B 17(3):601–607. https://doi.org/10.1007/BF02670227
32. Pang J, Hu S, Shen J, Wang P, Liang Y (2016) Arc characteristics and metal transfer behavior of CMT + P welding process. J Mater Process Technol 238:212–217. https://doi.org/10.1016/j.jmatprotec.2016.07.033
33. Rokhlin S, Guu A (1993) A study of arc force, pool depression, and weld penetration during gas tungsten arc welding. Weld J 72(8):381S–390S